

Characterization of the latent image to developed image in model EUV photoresists

John T. Woodward¹, Kwang-Woo Choi^{2,3}, Vivek M. Prabhu², Shuhui Kang²,
Kristopher Lavery², Wen-li Wu², Michael Leeson³, Anuja De Silva⁴,
Nelson M. Felix⁴, Christopher K. Ober⁴

¹*Optical Technology Division and* ²*Polymers Division,*
National Institute of Standards and Technology, 100 Bureau Dr. Gaithersburg, Maryland 20899

³*Intel Corporation, 2200 Mission College Blvd, Santa Clara, California 95054*

⁴*Cornell University, Materials Science & Engineering, 310 Bard Hall,*
Ithaca, New York 14853-1501

ABSTRACT

Current extreme ultraviolet (EUV) photoresist materials do not yet meet performance requirements on exposure-dose sensitivity, line-width roughness, and resolution. In order to quantify how these trade-offs are related to the materials properties of the resist and processing conditions, advanced measurements and fundamental studies are required that consider EUV-resist specific problems. In this paper, we focus on the correlations between the latent image and developed image in EUV exposed line/space features. The latent images of isolated lines produced by EUV lithography are characterized by atomic force microscopy through the change in topology caused by change in film thickness that occurs upon deprotection. The resulting latent-image deprotection gradient (DG_L), based on line cross-sections, and latent-image line-width roughness (LWR_L) provide metrics and insight into ways to optimize the lithographic process. The results from a model poly(hydroxystyrene-co-*tert*-butylacrylate) resist and a model calix[4]resorcinarene molecular glass type resist show the general applicability of the metric before development.

Keywords: atomic force microscopy, EUV photoresists, latent image, line width roughness

1. INTRODUCTION

Current EUV photoresist materials must simultaneously meet dose sensitivity, line-width roughness (LWR) and resolution performance requirements for implementation in sub-32 nm lithography. Development of advanced chemically amplified photoresists includes optimizing formulations for photoresist chemical composition, photoacid generator, and base quencher additive. This approach typically is done with full-scale photolithography using standard development and analysis of line/space features in terms of critical dimension and line-width roughness as a function of dose and focus. However, due to a lack of sufficient specialized facilities such as EUVL steppers, micro-exposure tools, or interferometric lithography tools this approach may not be immediately feasible as was testing with 193 nm lithography. Independent of either DUV or EUV lithography the quality of the latent image and mechanism of development are general to the lithographic process and impact feature fidelity, such as LWR.

Materials causes of line-width roughness are due to the interdependent photolithography process steps, which can be separated into two groups, those that define the internal deprotection interface (latent image) and those that control the dissolution process (development). The first includes the important details concerning the exposed aerial image, photoacid generation mechanisms, and during the bake step, photoacid reaction and diffusion which results in an image blur effect. The photoresist chemistry and mechanisms of controlling the latent image quality have been established for polymer photoresists with quantitative measurements and model materials.¹ The aqueous hydroxide development step,

controlled by photoresist composition and developer strength, remains strongly dependent upon the latent image which defines a small fraction of resist material which may swell, but not dissolve as recently observed.^{2,3}

This paper focuses on using a unique EUV facility and performing a systematic study of the latent image of isolated lines from 100 nm to 20 nm. Latent images have been examined previously with near-field Fourier transform vibrational spectroscopy⁴, scanning electron microscopy⁵, neutron reflectivity^{6,7,8,9,10}, and scanned probe methods.^{11,12,13,14} We use atomic force microscopy (AFM) (a scanned-probe technique) to image the topology of EUV lithography exposed, but not developed, model resists in order to identify sources of LWR. AFM provides a non-destructive, high resolution technique with topological and spatial sensitivity to characterize the latent image. While AFM has been used in limited capacity specifically as a CD metrology, we demonstrate its applicability as a measurement method to quantify the latent image deprotection gradient (DG_L) and line-width roughness (LWR_L). We are able to test the hypothesis that a higher DG_L leads to improved LWR_L . However, we uncover that the trends do not map to the developed LWR. We demonstrate that both a model polymer ESCAP and molecular glass resist have similar behavior despite their very different architectures. Therefore, we conclude that the choice of molecular architecture does not fundamentally improve the quality of the latent image and elimination of LWR. By measuring the DG_L , one may develop a resist independent parameter to compare the relative merits of different resist platforms.

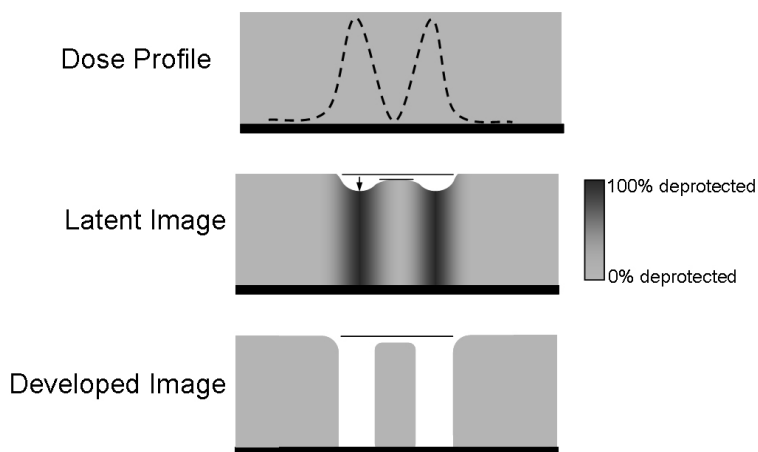


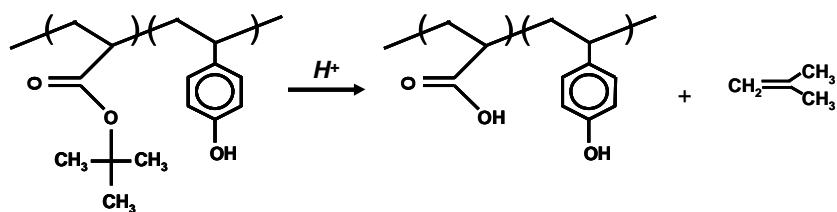
Figure 1. Schematic of the lithography process highlighting a change in film thickness due to deprotection. The height change in the latent image is proportional to deprotection extent which is profiled by AFM for isolated lines.

2. METHODOLOGY[†]

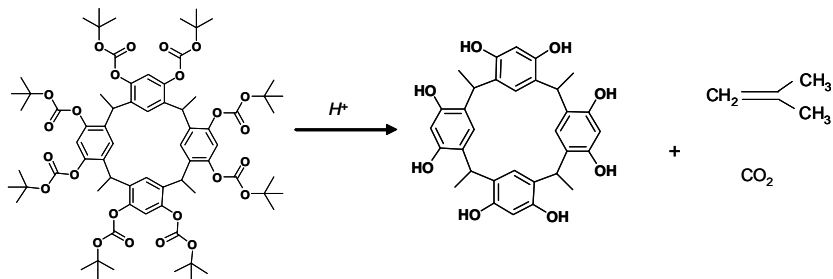
2.1 Model Resists

Two architectures of photoresists were examined. The first was a model polymeric ESCAP-type resist¹ consisting of a 49:51 poly(hydroxystyrene-co-*tert*-butylacrylate).^{8,15} The second was a calix[4]resorcinarene molecular glass (MG) type resist fully protected with *tert*-butoxycarbonyl (t-BOC) groups.¹⁶ Schematics of the acid catalyzed reaction for both architectures are shown in Figure 2. Both resists were formulated with 5 % by mass triphenylsulfonium perfluorobutanesulfonate (TPS-PFBS) photoacid generator without any base additives. All samples were spun cast onto hexamethyldisilazane primed silicon wafers from solutions of propylene glycol methyl ether acetate to a thickness of 100 nm followed by post apply bake for 60 s at 130 °C for model ESCAP and 60 s at 100 °C for MG. A post exposure bake (PEB) at 90°C for 30 s was performed on both samples.

[†] Certain commercial equipment, instruments, or materials are identified in this paper to specify the experimental procedure adequately. Such identification is not intended to imply recommendation or endorsement by the National Institute of Standards and Technology, nor is it intended to imply that the materials or equipment identified are necessarily the best available for the purpose.



(a) Model ESCAP



(b) t-BOC protected calix[4]resorcinarene molecular glass

Figure 2. Acid catalyzed deprotection reaction of (a) poly(hydroxystyrene-*co-tert*-butyl acrylate) P(HOST-*co*-tBA) – Model ESCAP and (b) Calix(4) resorcinarene-t-BOC (Molecular Glass)

2.2 Exposure

Samples were exposed at the Lawrence Berkeley National Laboratory (LBNL) Advanced Light Source 0.3 NA (numerical aperture) EUV micro-field exposure tool (MET) with annular illumination (0.3 / 0.55).^{17,18} A series of exposures in 1 mJ/cm² steps and several focuses were taken on each sample. A dark field mask consisting of a variety of test patterns was used. After resist film preparation, post-apply, and post-exposure bake the samples were returned to NIST for analysis of the latent images prior to development. One sample was developed at LBNL to determine best focus.

2.3 Latent and Developed Image Analysis

Latent images were analyzed using an atomic force microscope (MFP-3D, Asylum Research) in intermittent contact mode using silicon tips with a spring constant of 16 N/m and a radius of curvature < 10 nm. For developed images, tips with an electron-beam deposited, amorphous carbon spike (DP14/sting, MikroMasch) with a 5 N/m spring constant and 4 nm radius of curvature were used. These tips have an aspect ratio of at least 4:1 that allows improved imaging of the 100 nm deep trenches found on the developed samples. Samples were dried under nitrogen before imaging to reduce long range attractive forces.

Images were taken of isolated lines with nominal widths of 20 nm, 40 nm, 60 nm, and 100 nm over a range of exposure doses at optimal focus. 1 micron wide and 2 micron tall images were taken with 1024 points along each scan line and 512 scan lines. Thus the pixel density is approximately 1 nm/pixel for each scan across the line with each scan line taken every 4 nm along the lithographic feature. After the latent image data was collected, the samples were developed in 0.26N TMAH for either 30 s (MG) or 20 s (ESCAP). The developed samples were imaged at the same locations in intermittent contact mode. Unfortunately, due to problems with adhesion and line-collapse a systematic study of the model MG developed images was not possible.

Images were processed using the MFP-3D analysis software in IGOR (Wavemetrics) to plane fit and flatten the images. A routine based on the work of Villarubia¹⁹ was used to deconvolute the tip shape from the latent and developed

topography images. This code creates a blind reconstruction of the tip with no initial assumptions about the tip shape, by using information contained in the images taken with the tip. Typically, several images were used to construct the tip and then the tip was deconvolved from all the images taken with that particular tip to create an eroded image. These eroded images were then analyzed using SuMMIT (EUV Technology) to determine LWR and LWR power spectrum density (PSD) for both the latent and developed images. A sigmoidal edge detection method with 50 % threshold setting was used to obtain 3σ LWR. We found varying the threshold between 30 % and 80 % had a minimal effect on LWR measurements.

3. RESULTS AND DISCUSSION

3.1 Latent Images and Cross-Sections

AFM images of the samples after EUV exposure and PEB showed significant topography due to mass loss in the exposed regions. Figure 3 shows a typical series of AFM images of isolated lines from the iso-dense region of the test mask. Typically, the latent image of the lines could be observed for a wide range of exposures that extended well beyond the range of the lines found in the developed samples. Figure 4 shows a series of cross-sections of the latent image of lines with target CDs of 20 nm, 40 nm, 60 nm, and 100 nm for exposures from 3 mJ/cm^2 to 6 mJ/cm^2 . This exposure range fell within the process window for the 100 nm lines.

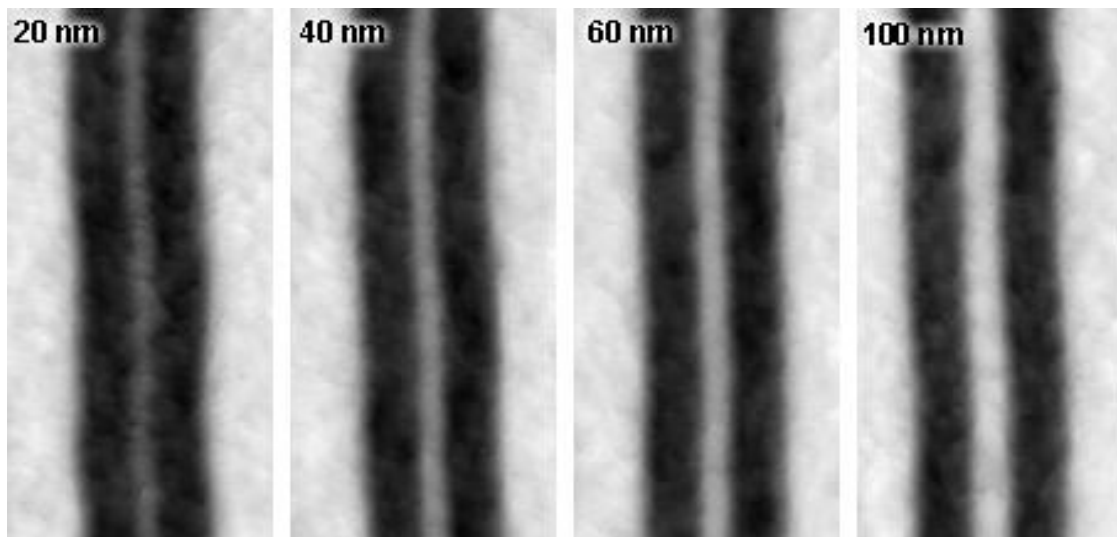


Figure 3. AFM latent images of dark field isolated lines in the model ESCAP resist. Nominal CD appears in upper left corner of each image. While all lines are seen in the latent image, only the 60 nm and wider lines remain after development at this dose. Exposure was 4 mJ/cm^2 . PEB was 90°C for 30 s. Images are 1 micron by 2 microns with a 20 nm black to white z-scale.

There are several features of the cross-sections that are common to both the model ESCAP and MG resists. For a given exposure dose the depth of the exposed regions is the same for all the line widths. This depth gets progressively lower for higher exposure doses until a plateau is reached. A small film loss appears even at the center of the lines (top loss). This loss increases with increasing dose and for a given dose is greater for narrower lines. Thus, there is a degree of top loss/ top rounding that is present in the latent image.

Using images of high exposure samples with long PEB times, we were able to determine that full deprotection leads to a 23 % reduction in film thickness for the model ESCAP resist and a 57 % reduction in film thickness for the MG resist. We will proceed with the assumption that loss in film thickness is linearly proportional to the deprotection fraction in the underlying film and thus that the AFM topography data of the latent images provides a measure of the deprotection fraction of the resist as indicated by the deprotection % on the right hand axes of the latent image cross-sections in Fig. 4.

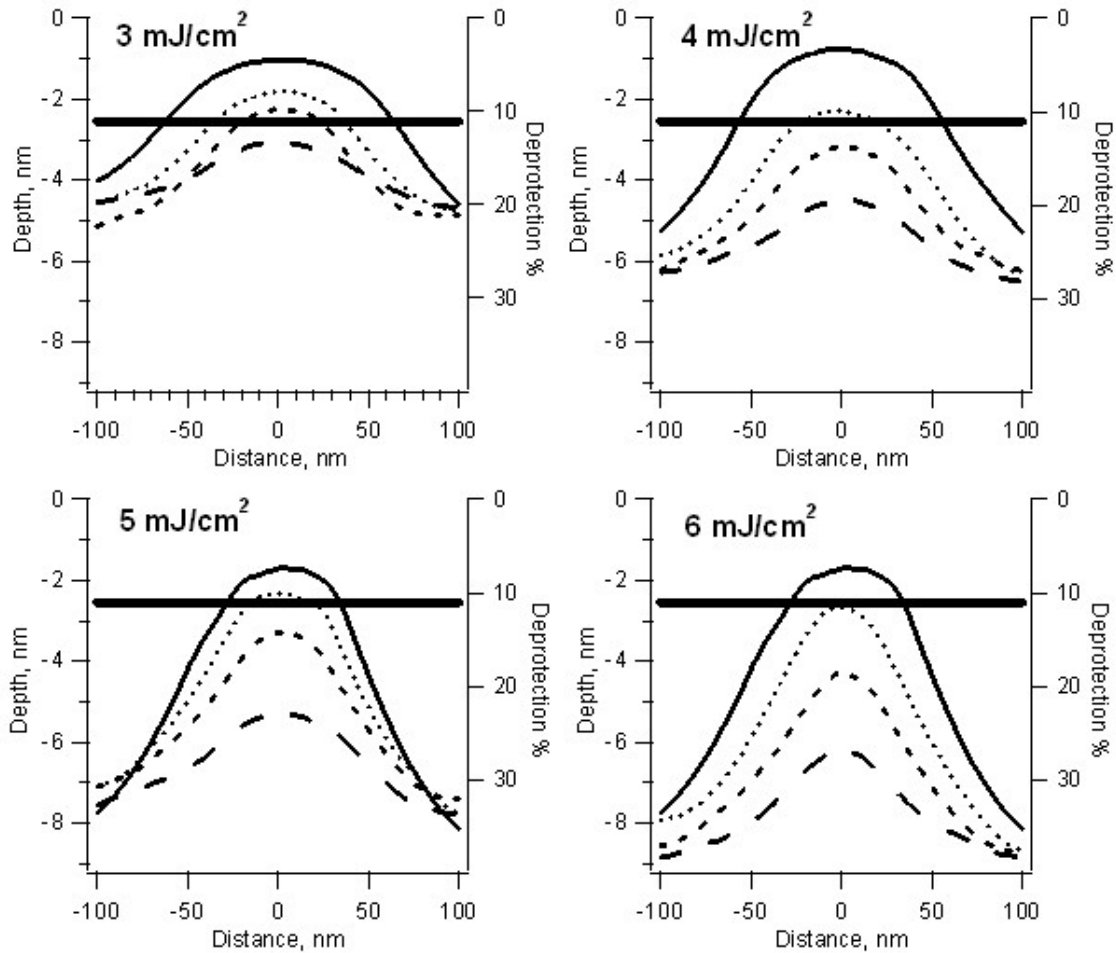


Figure 4. Cross-sections of the latent images of 100 nm (solid), 60 nm (dotted), 40 nm (small dash) and 20 nm (large dash) isolated lines in the model ESCAP resist at various exposures. The depth is relative to resist level outside the exposed region, so all lines show some top loss in the latent image with the loss increasing at higher doses and for narrower lines. The horizontal line represents the deprotection level of the solubility switch as determined by which lines appear in the developed images. Isolated lines with a cross-section that peaks above this level print, while those with latent image profiles below do not.

3.2 Deprotection Gradient

We define the latent image deprotection gradient, DG_L , as the absolute value of the derivative of the deprotection fraction with respect to distance. The assumption that the topography change due to mass loss in the film is directly proportional to the deprotection fraction, ϕ , allows us to directly compute DG_L from a topography cross-section of the latent image where the proportionality constant, C , is derived from the mass loss at full deprotection.

$$DG_L \equiv \left| d\phi/dx \right| \equiv C \left| dz/dx \right| \quad (1)$$

As an example, Fig 5a and 5c show the cross-sections for the latent images of 20 nm, 40 nm, 60 nm, and 100 nm isolated lines for both the model ESCAP (a) and MG (c) resists exposed at 4 mJ/cm^2 with a $90^\circ\text{C}/30 \text{ s}$ PEB. Fig 5b and 5d show the corresponding plots of the deprotection slope vs. deprotection fraction calculated from fits to the line feature. The analysis of the latent image shows that the DG_L is zero at the bottom of the space where there is maximum deprotection and at the top of the line. The DG_L displays a maximum in between the bottom of the space and top of the line with the peak height and location depending on the details of the deprotection profile. For the isolated lines, the deprotection

fraction in the exposed areas is the same for each of the line widths. So, all the curves for each resist end at same deprotection fraction: $\phi = 0.28$ for the model ESCAP and $\phi = 0.61$ for the MG. The curves begin at the deprotection fraction at the top of the line, which for the 100 nm lines in both resists is near $\phi = 0$. The narrower lines have progressively more deprotection in the unexposed regions, due to aerial image quality and acid diffusion, and thus their curves begin at progressively higher values of ϕ . In general, the narrower lines have a smaller peak in the DG_L .

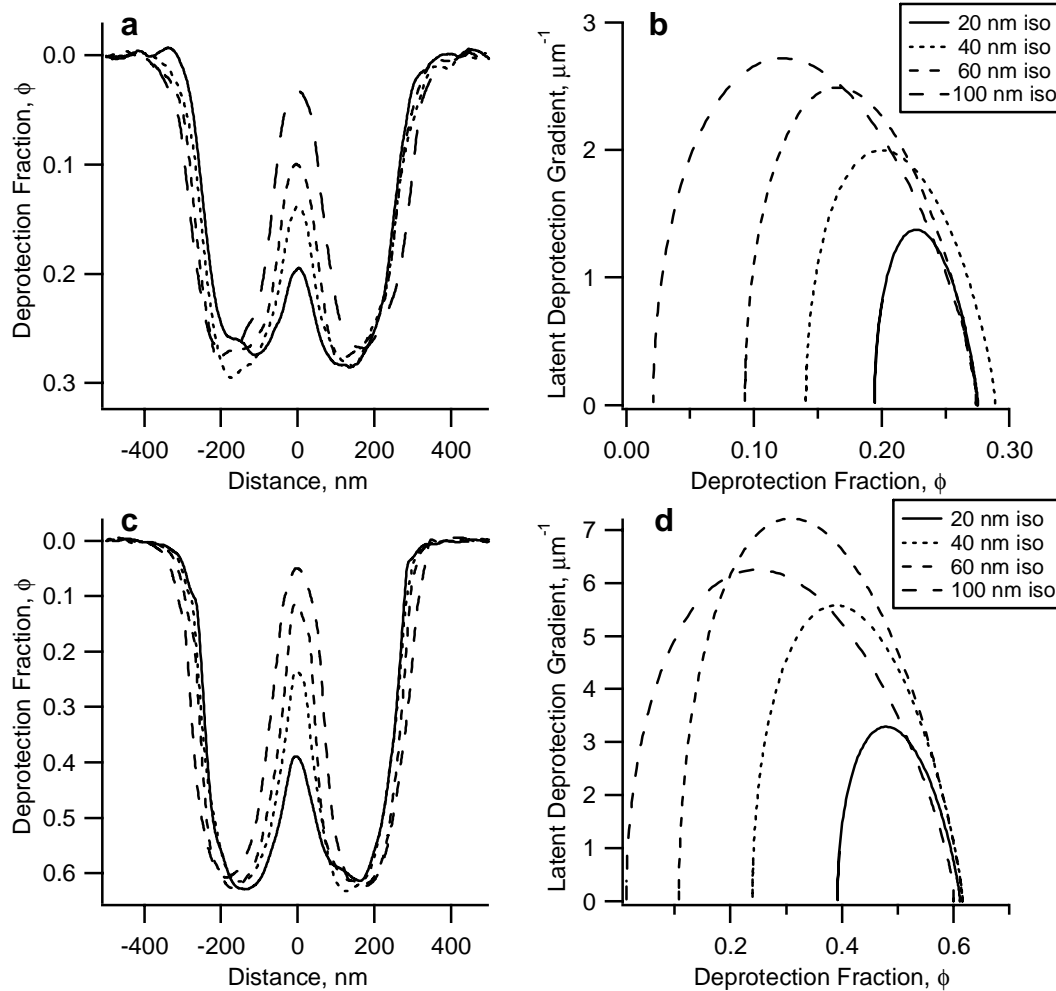


Figure 5. Cross-sections of latent images of 20 nm, 40 nm, 60 nm, and 100 nm lines exposed at 4 mJ/cm^2 with a 30 s PEB at 90°C for the model ESCAP (a) and MG (c) resists. The different reaction rates and diffusion parameters for the two resists lead to a much greater deprotection extent in the exposed areas for the MG resist for the same exposure and PEB. The deprotection fraction is the extent of deprotection normalized to 1 for complete deprotection and 0 for the unexposed resist. (b) and (d) plot of the DG_L vs. deprotection fraction based on a Gaussian fit to the center peak of the latent image cross-sections in (a) and (c) respectively. Calculating the DG_L based on the Gaussian fit reduces the noise and highlights the more general features of the DG_L curves.

To test the hypothesis that a higher DG_L leads to improved line quality we plotted DG_L vs. LWR_L in Figure 6. We can see that low values of DG_L lead to large LWR_L , while high values lead to reduced LWR_L . However, the rate of improvement at high DG_L diminishes. For example, from Fig 5 we can see that at 4 mJ/cm^2 the peak DG_L for the MG is roughly twice that for the model ESCAP. For the 20 nm lines, with DG_L of 1.4 in the model ESCAP and 3 in the MG, this leads to an improvement in the LWR_L from 40 nm to 25 nm. While for the 100 nm lines, with DG_L of 2.6 in the model ESCAP and 6 in the MG, the LWR_L only improves from 13.2 nm to 10.5 nm. We can see that that both the model ESCAP and MG resist have similar behavior despite their very different architecture leading us to speculate that DG_L may be a resist independent parameter that is useful for comparing the relative merits of different resist platforms.

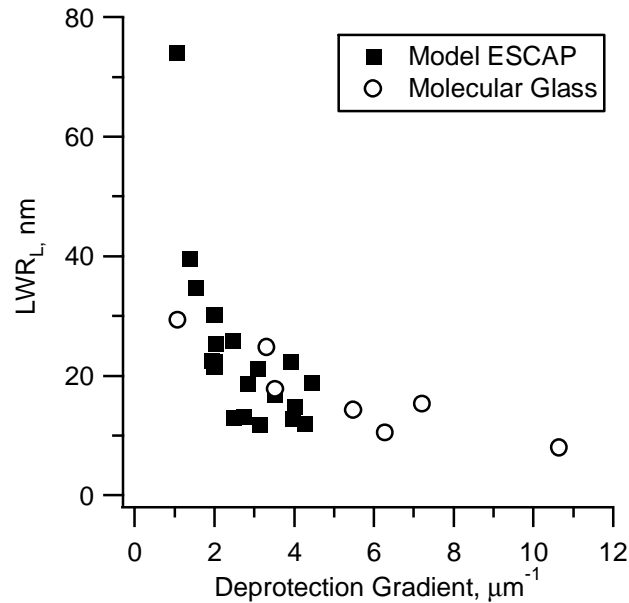


Figure 6. Plot of latent image deprotection gradient vs. latent image LWR.

In Figure 7, we plot the DG_L curves for the 20 nm iso lines in the model ESCAP resist for exposures 3 mJ/cm^2 through 7 mJ/cm^2 . As the dose increases the curves shift to higher deprotection levels as would be expected. In addition, both the width of the curves and the maxima of the curves increase at higher dose. Note that all of these curves have a range for the deprotection fraction that is greater than the solubility switch ($\phi = 0.11$) and thus none of the 20 nm lines remained after development. There were no features visible after development at the 2 mJ/cm^2 exposure leading us to conclude that this level of exposure did not lead to a deprotection fraction greater than the solubility switch ($\phi = 0.11$).

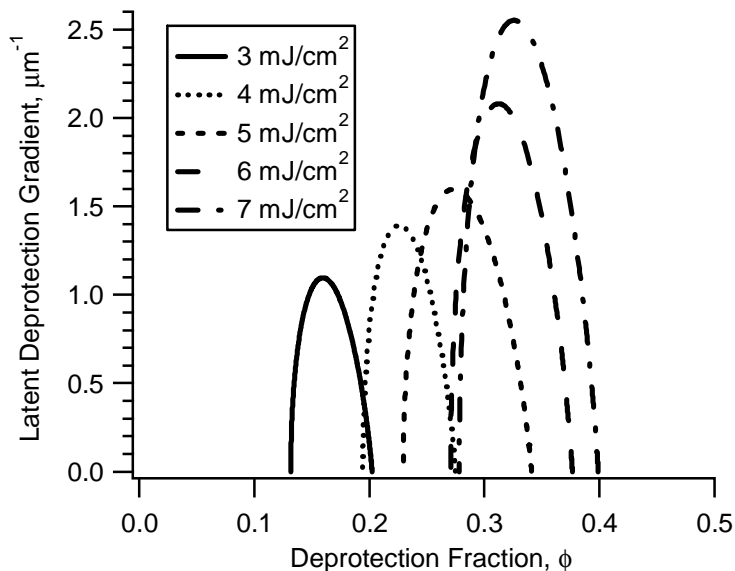


Figure 7. Deprotection gradient vs. deprotection fraction for 20 nm isolated lines in model ESCAP resist with a 30 s PEB at 90°C for a series of doses from 3 mJ/cm^2 to 7 mJ/cm^2 .

While none of the 20 nm lines printed, the latent images of the lines were easily imaged with the AFM and the family of DG_L curves provides insights into optimizing the process window. First, we note that at lower doses the curves become less overlapped leading to the possibility, as found here, that the solubility switch does not intersect with any of the curves. This leads to a failure to print the line despite the existence of viable latent images. If the solubility switch were

known (and fixed), one could optimize the dose to match the peak of the DG_L curve at the solubility switch. From the existing curves and solubility switch of $\phi = 0.11$, we would predict that this would yield a curve with a maximum DG_L of only about $1 \mu\text{m}^{-1}$. Additionally, the curve would be narrowly peaked so that small changes in dose or the solubility switch would lead to large reductions in the effective DG_L and the consequent degradation in the printed feature. If one could arbitrarily choose or shift the solubility switch to higher deprotection levels to intersect the higher dose curves, one potentially has access to higher DG_L values and therefore process conditions for improved feature quality. Similarly, it is possible to investigate how changes in other process conditions such as PEB time or temperature influence the DG_L curves.

3.3 Latent Image LWR_L Power Spectrum Density: Model ESCAP and MG

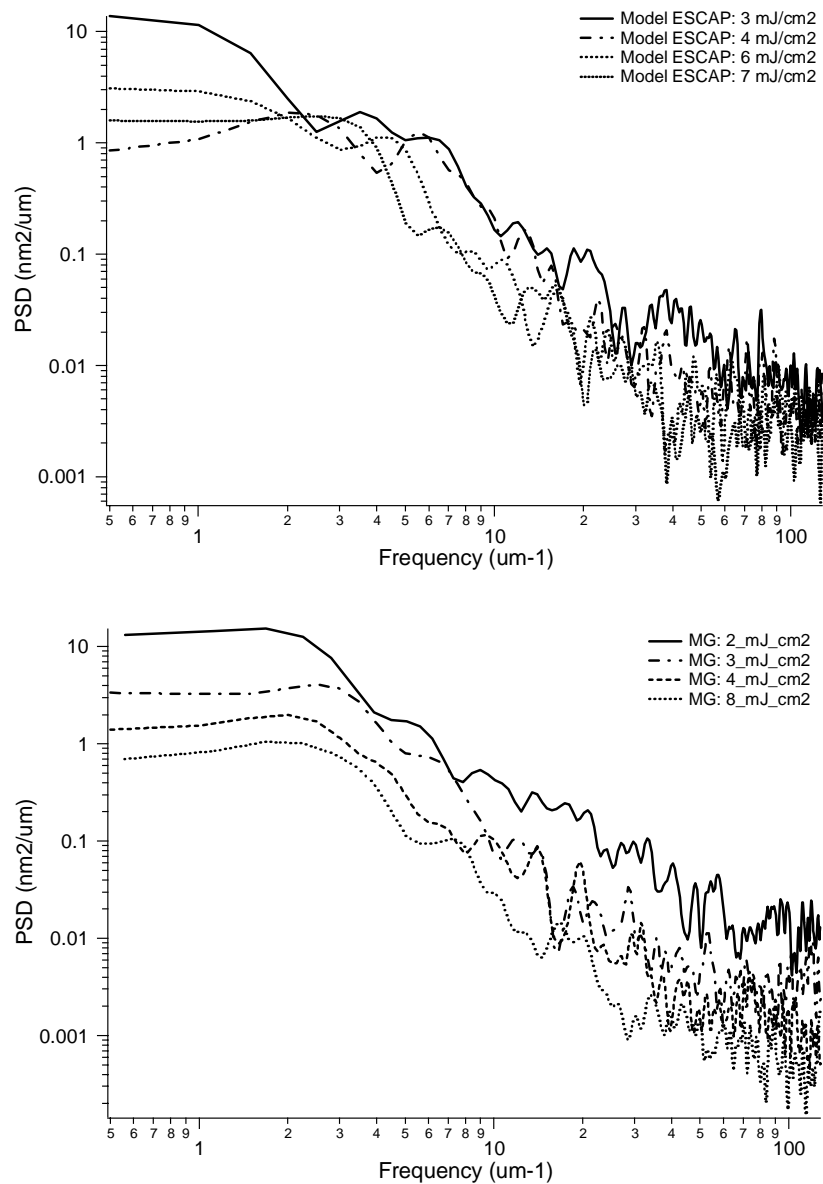


Figure 8. EUV dose effect on the latent image LWR_L PSD (power spectrum distribution) for the Model ESCAP and MG (100nm Isolated Line)

The effect of dose (Figure 8) on the latent image of 100 nm isolated line LWR_L wavelength shows different response between model ESCAP and MG. The power spectrum for MG shows that the LWR_L wavelength in the (10 to 500) nm range is modulated by an increase in EUV dose from (2 to 8) mJ/cm^2 for MG. On the other hand, the model ESCAP shows mid-to-low frequency LWR_L components in wavelengths less than (50 to 100) nm upon increasing the EUV dose. The apparent photoacid diffusion constant, D , in the MG was measured to be faster ($D_{MG} = (3 \text{ to } 5) \times D_{ESCAP}$) than model ESCAP at equal processing conditions²⁰ and therefore could benefit from an acid diffusion smoothening effect on LWR_L . Ishida²¹, reported previously that calixarene materials exhibited peak LWR wavelength range of (10 to 100) nm similar to the length scale observed in this study.

3.4 Latent to Developed Image LWR Power Spectrum Density: Model ESCAP

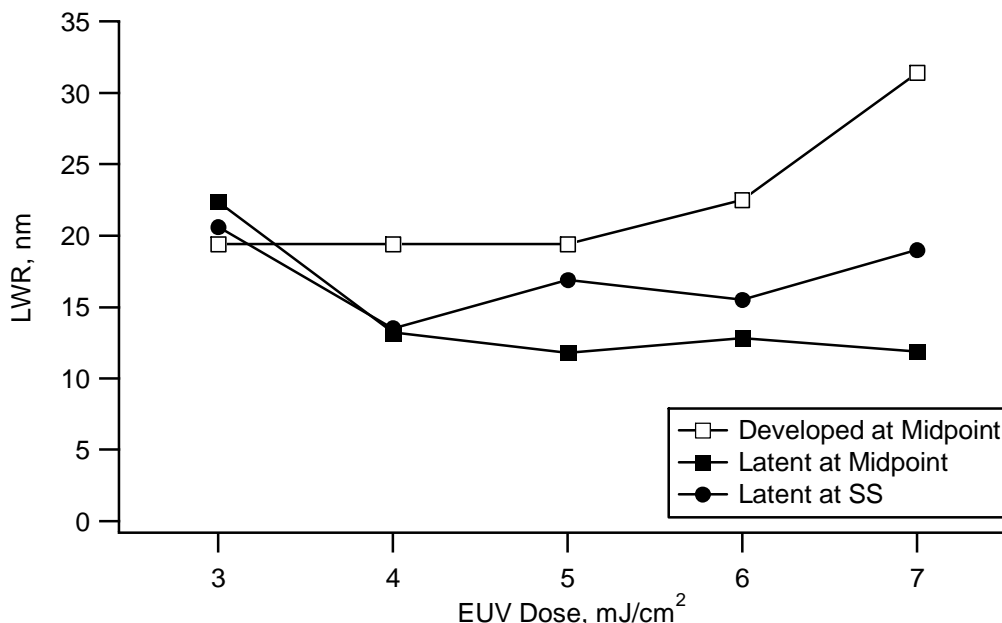


Figure 9. Comparison of latent to developed image LWR of 100nm isolated line for the Model ESCAP after 0.26N TMAH development as a function of dose. The latent LWR was calculated both at the midpoint of the line as well as a point approximating the location of the solubility switch.

The general trend for the latent (LWR_L) and developed image (LWR_D) line width roughness with EUV dose for 100 nm isolated lines is shown in the Figure 9. AFM images were taken from identical patterns before and after 0.26N TMAH development. The latent image LWR_L decreases rapidly initially with EUV dose from greater than 20 nm to (11 to 13) nm and remains relatively unchanged with further increase in the EUV dose up to 7 mJ/cm^2 . On the other hand, developed image LWR_D is initially lower than the latent image LWR, but becomes larger with increasing EUV dose. The developed image LWR continues to increase for EUV exposure dose $(2 \text{ to } 3) \times E_0$ the nominal dose to clear (E_0). An exact quantitative comparison between latent to developed image LWR as determined by AFM is very difficult at this stage and its results should be used with caution, since there may be systematic differences in analyzing the shallower latent image topography and the deeper, more steeply sloped features of the developed images. We speculated that the increase in LWR_D at higher dose may reflect the shift of the top of the line closer to the solubility switch, as seen in Fig 3, and thus away from the optimal DG_L for that feature. To test this we looked at the LWR_D as we varied the threshold level at which it was calculated. However, the LWR analysis of the sensitivity to the edge detection threshold % setting from 30 % to 80 % found a minimal effect and did not change these trends. Even with the threshold set to 90% of the line height (the approximate location of the solubility switch) on the 7 mJ/cm^2 feature, the increase in LWR_L is small compared to the increase in LWR_D . Thus LWR_L is not predictive of LWR_D and development effects can significantly degrade feature quality.

At a very low EUV dose, the latent image LWR_L is larger than the developed image LWR_D . A developer process can contribute to a smoothing effect²² at the latent line edge boundary by removing areas of lower deprotection heterogeneity sites making the developed image LWR smaller than the latent image LWR . AFM images obtained from model ESCAP clearly highlight difference in the EUV exposed areas (space) of (1 to 2) mJ/cm^2 versus (3 to 5) mJ/cm^2 . At mid EUV doses, the latent image LWR_L continues to decrease with dose as the deprotection gradient slope increases. It is related to an acid diffusion smoothing effect observed by others^{23,24}, but a developed image LWR_D is always greater than the latent image LWR for a given EUV dose. We speculate this direct transfer of latent to develop line fidelity is due to undesirable swelling and developer penetration into the underlying line/space feature. At higher EUV doses, the latent image LWR_L reaches a plateau with increasing EUV doses, but the developed image LWR_D continues to increase. At this point the chemical contrast of the resist at the line edge is decreasing due to inter-diffusion of photoacid to the unexposed area of resist. This causes dark erosion and a solubility switch point shifting closer to the top/peak of deprotection line edge profile. This was confirmed by reaction-kinetics modeling and observed by the increasing film loss of the line. Therefore at higher EUV doses the developer process contributes to degrading the line edge profile, due to the dark erosion of the line, causing a significant increase in the developed imaged LWR_D .^{25,26}

An example, the model ESCAP LWR PSD before and after development is shown in the Fig. 10 for 100 nm isolated line at $5 mJ/cm^2$. After development, mid-to-low frequency (greater than 100 nm spatial period) LWR appears to be affected by development process.

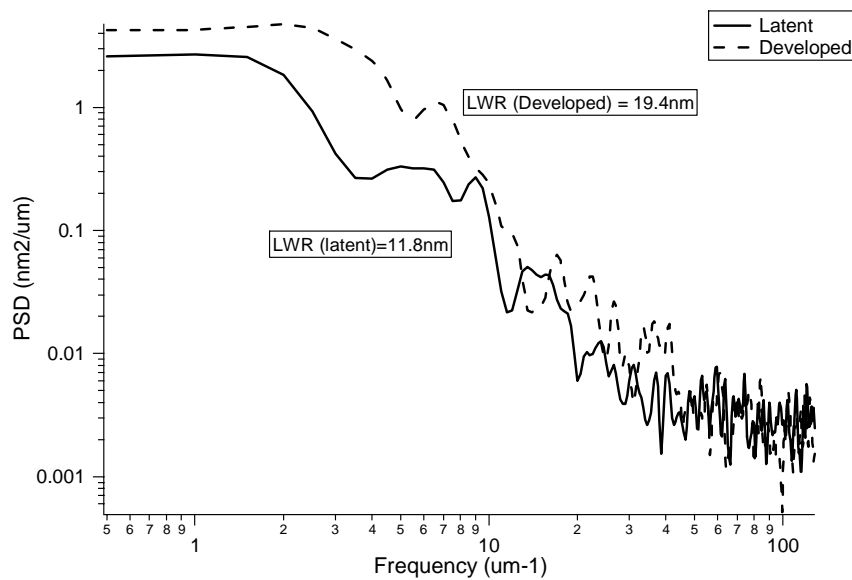


Figure 10. Model ESCAP's 100 nm isolated line LWR PSD comparison before (latent image) and after development for the EUV dose $5 mJ/cm^2$. Prior to development (latent image) $LWR = 11.3 nm$ compared to $19.4 nm$ after development.

4. CONCLUSIONS

AFM images of latent images of EUV exposed photoresist show topographic features related to the deprotection level of the resist. The latent images of features as small as 20 nm are clearly resolved by AFM over a wide range of exposures despite these features not appearing after development. The deprotection gradient serves as a quantitative measure of the latent image quality with larger slopes indicating higher quality. This approach complements the understanding of the effect of image log slope, but in the latent image. Comparison of latent image LWR for the polymeric (model ESCAP) and molecular glass (calix[4]resorcinarene) photoresist with identical photoacid generator exhibited similar dependence on the deprotection gradient. AFM measurement of the latent image deprotection gradient derived here is in very good agreement to deprotection reaction-diffusion kinetics of the model ESCAP and MG derived by other methods²⁰. These latent images provide alternative approaches to derive reaction kinetic parameters including acid diffusion constants and heuristics for matching image contrast to a desired solubility switch point. Knowledge of the deprotection profile in the

sub-32 nm latent image allows insight into how processing contributes to LWR. Further rational designs to other process steps such as development and resists architecture choice may be made based upon these latent images and develop schemes to resolve features unattainable by standard protocols.

5. ACKNOWLEDGEMENTS

This work was supported by a cooperative research and development agreement between Intel Corporation and NIST (NIST CRADA #CN-1892 and 1893). We also would like to acknowledge Manish Chandhok, Wang Yueh, Todd Younkin, Melissa Shell, George Thompson, and Christof Krautschik from Intel, and Chris Soles and Eric Lin from NIST for their support. Jim Sounik, Matthew Romberger, and Michael Sheehan at DuPont Electronic Materials provided the polymer used in this study. Excellent support provided by the staff at LBNL ALS (Patrick Naulleau, Paul Denham, Brian Hoef, Gideon Jones, Jerrin Chiu) is also appreciated. We thank Stefan Vinzelberg at Atomic Force F & E (Germany) for the Igor code implementing the AFM tip deconvolution.

6. REFERENCES

1. Ito, H., "Chemical amplification resists for microlithography" *Advances in Polymer Science* **175**, 37-245, (2005).
2. Prabhu, V. M., Vogt, B. D., Kang, S., Rao, A., Lin, E. K., and Satija, S. K., "Direct measurement of the spatial extent of the in situ developed latent image by neutron reflectivity" *Journal of Vacuum Science & Technology B* **25**, 2514-2520, (2007).
3. Prabhu, V. M., Vogt, B. D., Kang, S., Rao, A., Lin, E. K., Satija, S. K., and Turnquest, K., "Direct Measurement of the in situ Developed Latent Image: the Residual Swelling Fraction" *Proceedings of SPIE* **6519**, 651910, (2007).
4. Dragnea, B., Preusser, J., Szarko, J. M., McDonough, L. A., Leone, S. R., and Hinsberg, W. D., "Chemical mapping of patterned polymer photoresists by near-field infrared microscopy" *Applied Surface Science* **175**, 783-789, (2001).
5. Stewart, M. D., Tran, H. V., Schmid, G. M., Stachowiak, T. B., Becker, D. J., and Willson, C. G., "Acid catalyst mobility in resist resins" *Journal of Vacuum Science & Technology B* **20**, 2946-2952, (2002).
6. Vogt, B. D., Kang, S., Prabhu, V. M., Lin, E. K., Satija, S. K., Turnquest, K., and Wu, W., "Measurements of the reaction-diffusion front of model chemically amplified photoresists with varying photoacid size" *Macromolecules* **39**, 8311-8317, (2006).
7. Vogt, B. D., Kang, S., Prabhu, V. M., Rao, A., Lin, E. K., Wu, W., Satija, S. K., and Turnquest, K., "Influences of base additives on the reaction diffusion front of model chemically amplified photoresists" *Journal of Vacuum Science and Technology B* **25**, 175-182, (2006).
8. Lavery, K. A., Choi, K. W., Vogt, B. D., Prabhu, V. M., Lin, E. K., Wu, W. L., Satija, S. K., Leeson, M., Cao, H., Thompson, G., Deng, H., and Fryer, D. S., "Fundamentals of the Reaction-Diffusion Process in Model EUV Photoresists" *Proceedings of the SPIE* **6153**, 615313, (2006).
9. Vogt, B. D., Kang, S., Prabhu, V. M., Rao, A., Lin, E. K., Satija, S. K., Turnquest, K., and Wu, W., "The deprotection reaction front profile in model 193 nm methacrylate-based chemically amplified photoresists" *Proceedings of the SPIE* **6153**, 615316, (2006).
10. Wu, W., Prabhu, V. M., and Lin, E. K., "Identifying materials limits of chemically amplified photoresists" *Proceedings of SPIE* **6519**, 651902, (2007).
11. Ocola, L. E., Fryer, D., Nealey, P., dePablo, J., Cerrina, F., and Kammer, S., "Latent image formation: Nanoscale topography and calorimetric measurements in chemically amplified resists" *Journal of Vacuum Science & Technology B* **14**, 3974-3979, (1996).
12. Ocola, L. E., Fryer, D., Reynolds, G., Krasnoperova, A., and Cerrina, F., "Scanning force microscopy measurements of latent image topography in chemically amplified resists" *Applied Physics Letters* **29**, 717-719, (1996).
13. Ocola, L. E., Cerrina, F., and May, T., "Latent image characterization of postexposure bake process in chemically amplified resists" *Journal of Vacuum Science & Technology B* **15**, 2545-2549, (1997).
14. Foucher, J., Pikon, A., Anded, C., and Thackeray, J., "Impact of acid diffusion length on resist LER and LWR measured by CD-AFM and CD-SEM" *Proceedings of the SPIE* 6923-45, (2007).
15. Choi, K. W., Prabhu, V. M., Lavery, K. A., Lin, E. K., Wu, W. L., Woodward, JT, Leeson, M., Cao, H., Chandhok, M., and Thompson, G., "Effect of photo-acid generator concentration and developer strength on the patterning capabilities of a model EUV photoresist" *Proceedings of SPIE* **6519**, 651943, (2007).
16. Dai, J., Chang, S., Hamad, A., Yang, D., Felix, N., and Ober, C., "Molecular glass resists for high-resolution patterning" *Chem. Materials* **18**, 3404-3411, (2006).
17. Naulleau, P., Cain, J. P., Anderson, E. H., Dean, K. R., Denham, P., Goldberg, K. A., Hoef, B., and Jackson, K. H., "Characterization of the synchrotron-cased 0.3 numerical aperture extreme ultraviolet microexposure tool at the Advanced Light Source" *Journal of Vacuum Science & Technology B* **23**, 2840-2843, (2005).

18. Naulleau, P., Goldberg, K. A., Cain, J. P., Anderson, E. H., Dean, K. R., Denham, P., Hoef, B., and Jackson, K. H., "Extreme ultraviolet lithography capabilities at the advanced light source using a 0.3-NA optic" *IEEE Journal of Quantum Electronics* **42**, 44-50, (2006).
19. Villarrubia, J. S., "Algorithm for Scanned Probe Microscope Image Simulation, Surface Reconstruction, and Tip Estimation" *NIST Journal of Research* **102**, 425, (1997).
20. Kang, S., Lavery, K. A., Choi, K. W., Prabhu, V. M., Wu, W. L., Lin, E. K., De Silva, A., Felix, N., and Ober, C., "A comparison of the reaction-diffusion kinetics between model EUV polymer and molecular glass photoresists" *Proceedings of the SPIE* **6923**, (2008).
21. Ishida, M., Kobayashi, K., Fujita, K., and Ochiai, Y., "Investigating line-edge roughness in Calixarene fine patterns using fourier analysis" *Japanese Journal of Applied Physics* **41**, 4228-4232, (2002).
22. Neurether, A. R. and Wilson, C. G., "Reduction in x-ray lithography shot noise exposure limit by dissolution phenomena" *Journal of Vacuum Science & Technology B* **6**, 167-173, (1988).
23. Henke, W. and Torkler, M., "Modeling line edge roughness in ion projection lithography" *Journal of Vacuum Science & Technology B* **17**, 3112-3118, (1999).
24. Kozawa, T., Yamamoto, H., Saeki, A., and Tagawa, S., "Proton and anion distribution and line edge roughness of chemically amplified electron beam resist" *Journal of Vacuum Science & Technology B* **23**, 2716-2720, (2005).
25. He, D. and Cerrina, F., "Process dependence of roughness in a positive-tone chemically amplified resist" *Journal of Vacuum Science & Technology B* **16**, 3748-3751, (1998).
26. Yoshizawa, M. and Moriya, S., "Study of the acid-diffusion effect on line edge roughness using the edge roughness evaluation method" *Journal of Vacuum Science & Technology B* **20**, 1342-1346, (2002).